*Geophys. J. Int.* (2004) **158,** 310–326 doi: 10.1111/j.1365-246X.2004.02285.x

# Coseismic slip resolution and post-seismic relaxation time of the 1999 Chi-Chi, Taiwan, earthquake as constrained by geological observations, geodetic measurements and seismicity

Anne Loevenbruck,[1] Rodolphe Cattin,[1] Xavier Le Pichon,[2] Stéphane Dominguez[3] and Rémi Michel[4]

[1] *Laboratoire de Géologie, Ecole Normale Supérieure, 24 rue Lhomond,* 75231 *Paris Cedex* 05, *France. E-mail: loeven@geologie.ens.fr*
[2] *Collège de France, 6, place Marcelin-Berthelot,* 75005 *Paris, France*
[3] *Laboratoire de Géophysique, Tectonique, Sédimentologie, Université Montpellier II, Place E. Bataillon,* 34095 *Montpellier Cedex* 5, *France*
[4] *Laboratoire de Détection et de Géophysique, Commissariat à l'Energie Atomique, Bruyères-le-Châtel, France*

Accepted 2004 February 20. Received 2004 February 18; in original form 2002 November 6

## SUMMARY

We analysed the surface displacements estimated by Global Positioning System (GPS) measurements and Système Probatoire d'Observation de la Terre (SPOT) image correlation and the seismicity change induced by the Mw =7.6 1999 September 20 Chi-Chi earthquake. We first modelled the seismogenic zone for which we introduced a realistic geologically constrained ramp and flat geometry, and estimated by joint inversion of the GPS and SPOT data the coseismic slip distribution, stressing the resolution of the model parameters. The fair adjustment indicates that the ramp and flat geometry is consistent with the geodetic measurement. The calculated coseismic slip increases both towards the surface and northwards with maximum slip of approximately 15 m, in good agreement with the observed surface rupture and previously obtained slip models based on seismic waveforms. This distribution may be represented to a good approximation by a linear increase of slip with a constant azimuth in the plate convergence direction. Special emphasis is given to the analysis of the model resolution, which sharply decreases with depth in spite of the exceptionally well distributed and high-quality inverted data. This resolution decrease, expected for any slip distribution based on surface observations only, led us then to examine the seismicity as independent data to test our model following the static stress triggering hypothesis. The model is accurately defined in terms of Coulomb stress change in the central part of the rupture where the fault geometry is well constrained by seismic profile. In contrast, at the southern and northern ends it is less appropriate, however the static stress triggering approach is not precise enough to determine whether fault geometry or slip distribution is less suitable. We thus conclude that the analysis of seismicity in terms of Coulomb stress change might not allow us to examine small-scale features of seismogenic zones. Finally, we discuss post-seismic relaxation from the temporal variation of seismicity rate. In contrast to the relaxation time of 0.23–0.90 yr inferred from post-seismic permanent GPS measurements, we found that the decay of aftershock sequence follows Omori's law with an 8–14 yr relaxation time. We suggest that this discrepancy results from the coexistence of several different processes, not all associated with the production of aftershocks.

**Key words:** aftershocks, Chi-Chi earthquake, inversion, model resolution, seismotectonics, slip distribution.



## 1 INTRODUCTION

Taiwan is located on the convergent boundary between the Philippine Sea Plate (PH) and the Eurasia Plate (EU) at the junction of the Manila and Ryukyu trenches (Fig. 1). From Taiwan to the northern Philippines, the rapid northwest motion of the PH, approximately 80 mm $yr^{-1}$, is accommodated by the eastward subduction of the South China sea along the Manila trench. This subduction underthrusts the Chinese margin beneath Taiwan Island and leads to the collision with the Luzon volcanic arc, the suture zone being located along the longitudinal valley fault (LVF), east of Taiwan.

 

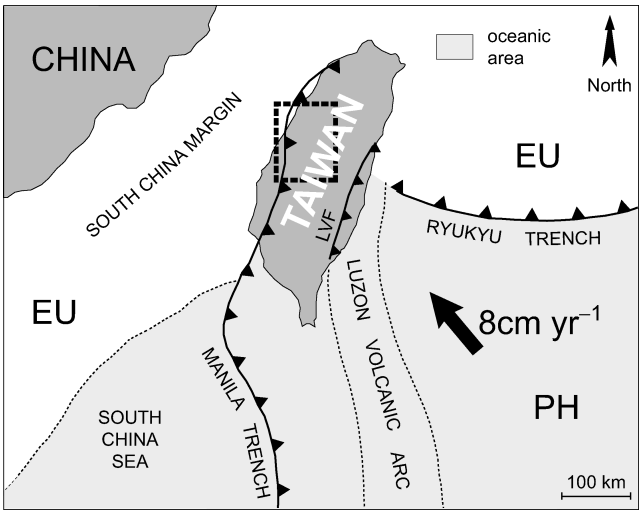


**Figure 1.** Geodynamic setting of Taiwan. LVF: longitudinal valley fault. Inset indicates the location of Fig. 2.

The obliquely thrusting Chi-Chi earthquake was the most recent large event produced by the subduction-collision process. It broke the Chelungpu thrust fault (CTF), a 30°E dipping splay fault emerging from the main decollement to the west of the Taiwanese accretionary wedge (Fig. 2). Because the wedge is onshore, this earthquake was probably the best-documented subduction earthquake in recent times. Prior to the earthquake, the CTF was identified as a potentially active range-front thrust, marking the boundary between the western foothills and the western coastal plain (see Kelson *et al.* 2001, for a review). This fault system also involves two other splay faults, the Shuangtung fault (Sh F) up to the foothills and the Changhua fault (Ch F) in the sedimentary plain (Figs 2 and 3; Suppe 1985, 1986). These two subparallel faults were not activated during the Chi-Chi earthquake (Rubin *et al.* 2001). Field surveys were conducted to map in detail the entire surface break of the CTF (e.g. Ma *et al.* 1999; Chen *et al.* 2001; Lin *et al.* 2001; Ouchi *et al.* 2001). In addition, two complementary methods of geodesy provide surface displacements on each side of the fault. On the one hand, the very precise but heterogeneously and non-densely distributed Global Positioning System (GPS) data (Yu *et al.* 1997, 2001) yield co- and post-seismic measurements. On the other hand, coseismic displacements are also estimated with larger uncertainties by correlation over a regular and dense grid between Système Probatoire d'Observation de la Terre (SPOT) images (Dominguez *et al.* 2003). In this paper:

(i) We discuss the constraints on the geometry of the CTF and we present the geodetic data (GPS and SPOT images).

(ii) We estimate a model of coseismic slip distribution by inversion of GPS and SPOT, and quantify its resolution. Several previous studies provided a slip distribution of the Chi-Chi earthquake using a small number of rectangular fault elements (e.g. Ma *et al.* 2000; Chi *et al.* 2001; Ji *et al.* 2001; Johnson *et al.* 2001). However, the oversimplification of the geometry in these previous approaches could introduce locally an incorrect definition of the rupture plane including overlaps and holes. Here, we have taken into account the complex 3-D fault geometry (including various dip angles and trends) constrained by a seismic profile and geological observations using more than 20 000 triangular fault elements. Moreover, the quantification of the model resolution allows us to discuss our results.

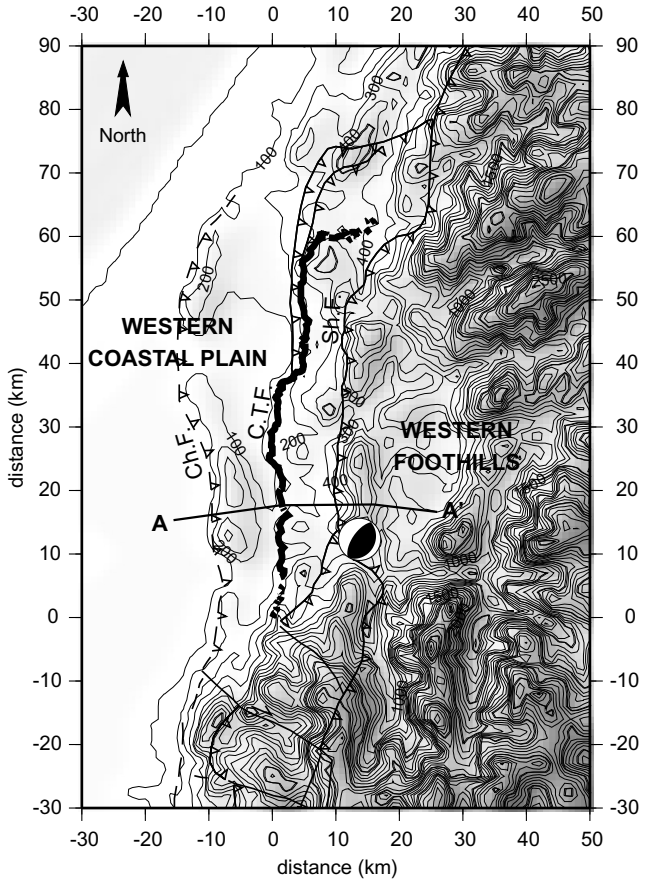


**Figure 2.** Topographic map of central Taiwan, contours every 100 m. Rupture trace along the CTF (black line) and fault plane solution (Harvard CMT) of the Chi-Chi earthquake, and neighbouring active faults (grey lines). Faults: Changhua fault (Ch F), Chelungpu thrust fault (CTF), Shuangtung fault (Sh F). The line A–A′ indicates the location of the cross-section of Suppe (1985) in Fig. 3.

(iii) We then examine the seismicity change as independent data to test *a posteriori* our model of slip distribution at depth following the static stress triggering approach and discuss this method.

(iv) We investigate the transient post-seismic deformation in terms of relaxation time from the seismicity and the post-seismic GPS observations.

## 2 GEOMETRY OF THE CHELUNGPU THRUST FAULT AND MEASUREMENTS OF COSEISMIC SURFACE DISPLACEMENTS

### 2.1 CTF geometry

The fault trace of the CTF has been mapped in detail: the main portion trends north–south over a distance of 60 km (Fig. 2). A balanced cross-section from Suppe (1981, 1985, 1986), based on geology and one seismic profile, has been used to obtain its structure at depth; Suppe showed the presence of an emerging thrust and a 6 km deep flat structure in the median portion of the CTF (Fig. 3). We extended the fault rupture to the east with a deeper ramp, which connects the 6 km deep flat to the 10 km deep decollement, which creeps during the interseismic period (Loevenbruck *et al.* 2001). The rupture trace bends eastwards at the northern end. It is associated with short

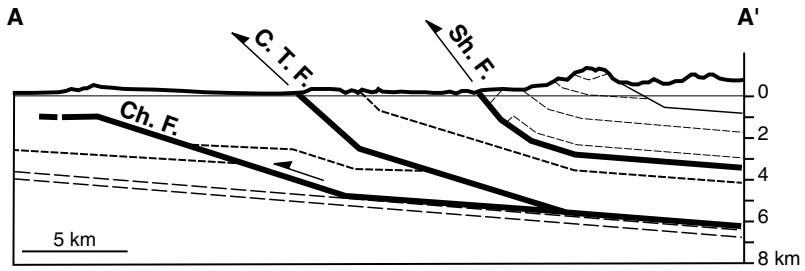


**Figure 3.** Cross-section across the western range-front modified from Suppe (1985). Black lines represent the main structures; the Changhua fault (Ch F), the Chelungpu thrust fault (CTF) and the Shuangtung fault (Sh F). The dashed lines indicate the bedding. See location in Fig. 2.

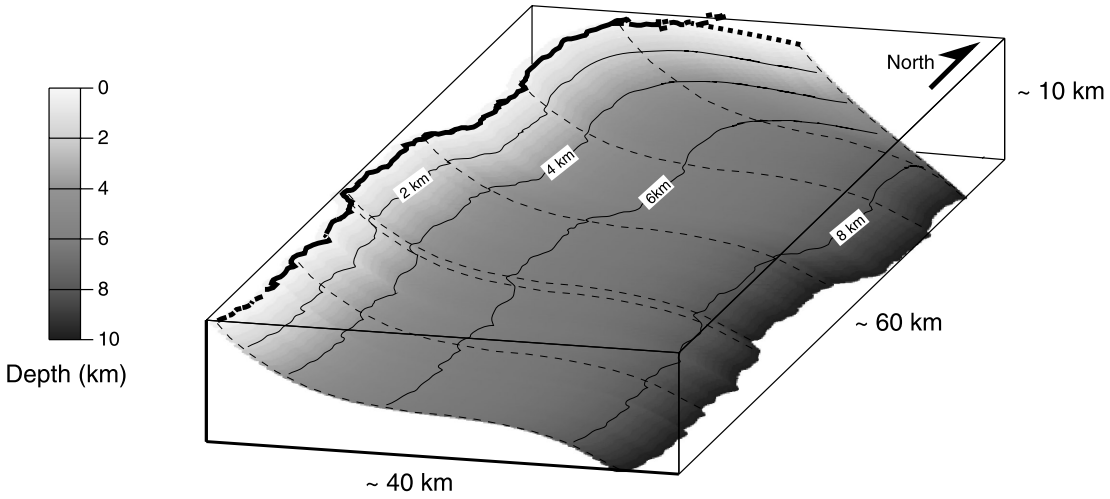


**Figure 4.** 3-D geometry of the broken CTF used in this study derived from structural cross-section (Suppe 1985) showing flat and ramp structure and the northern bend of the rupture.

anticlines and thrust faults (Chen *et al.* 2001; Lee *et al.* 2002). The deeper structure of this part of the fault is essentially unconstrained. The northern bend might reflect an E–W developing tear fault (Chen *et al.* 2001) connecting the CTF to the adjacent fault to the north. The fault rupture surface displayed in Fig. 4 was obtained by lateral extrapolation of the cross-section of Suppe, taking into account the geometry of the rupture trace. The computing scheme, developed to fully take into account this geometric complexity, is described in Section 3.1.

### 2.2 Coseismic surface displacements

The Central Geological Survey, the Satellite Survey Division, Land Survey Bureau and the Institute of Earth Sciences conducted the GPS project in Taiwan. The vertical and horizontal coseismic displacements measured at 142 GPS sites, including 45 permanent ones, (Yu *et al.* 2001) used in this study are shown in Fig. 5(a). In the vicinity of the fault break, the GPS sites on the footwall of the CTF are easy to distinguish from those of the hangingwall because of their small displacements, downward and southeastward, increasing near the rupture. On the hangingwall, the uplift and the eastward to northeastward displacements jointly decrease from the fault trace towards the east. The vertical components become negative and the horizontal ones are close to zero approximately 70 km east of the rupture trace. Close to the fault break, the uplift of the upper block is uneven.

Horizontal coseismic displacements derived from the subpixel correlation between two panchromatic SPOT images acquired 8 months before and 2 months after the Chi-Chi earthquake (Dominguez *et al.* 2003) were also used in the inversions. The coseismic offsets were measured from the phase shift of the Fourier transform of a sliding window. They were then compared and adjusted to the GPS data in order to provide constraints on the far-field displacements at the low spatial frequencies, not documented by the SPOT images. The complete method, developed by Van Puymbroeck *et al.* (2000), is detailed by Dominguez *et al.* (2003) for the Chi-Chi earthquake. The SPOT images correlation provides 2929 offset measurements every 160 m on a 60 × 60 km area (Fig. 5b). The discontinuity cutting through the displacement distribution marks the rupture fault trace. It separates the almost fixed footwall from the moving hangingwall. East of the rupture trace, the north and east components show a northeastward motion of the hangingwall, becoming more northward to the north. The SPOT data agree with the GPS measurements to indicate small southeastward displacements on the footwall, except in the middle portion of the fault break where the motion is northward.

Interferometric Synthetic Aperture Radar (InSAR) data recently published by Pathier *et al.* (2003) are not used for this study because these data are not available. In contrast with SPOT data, InSAR data give information only in the footwall area as a result of the phase decorrelation associated with the dense vegetation on the hangingwall. Thus, InSAR data are less essential than SPOT and GPS data to constrain the coseismic slip distribution of the Chi-Chi earthquake.

Two complementary sets of coseismic surface measurements are thus available. The SPOT method provides only horizontal components with relatively large minimal estimated errors of 0.20 m

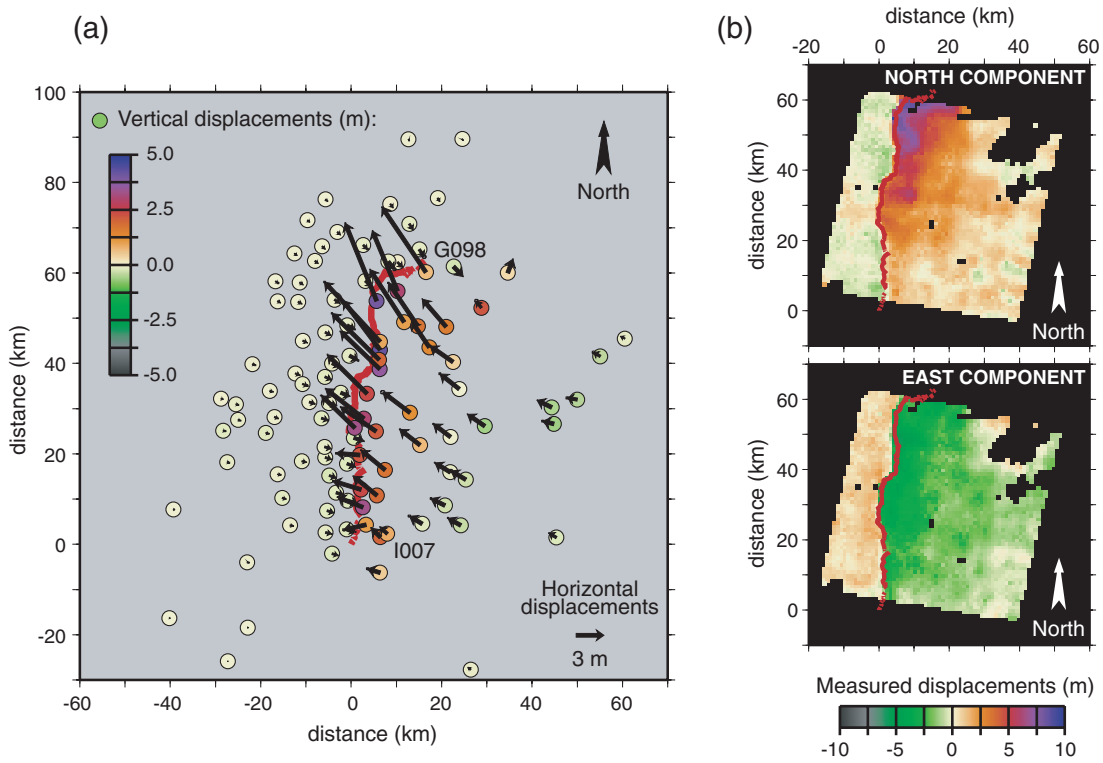


**Figure 5.** (a) Horizontal (vectors) and vertical (circles) coseismic GPS measurements related to the Chi-Chi earthquake (Yu *et al.* 2001). (b) North and east components of coseismic displacements related to the Chi-Chi earthquake estimated by SPOT images correlating (Dominguez *et al.* 2003). Red line indicates the surface rupture.

(Van Puymbroeck *et al.* 2000), but the SPOT data are numerous and regularly distributed around the fault trace. On the other hand, the sparser GPS data are three-component measurements. As the supplied GPS errors are formal errors and the SPOT ones are real uncertainties on displacement estimations, they have different meaning: the GPS errors are underestimated and were therefore multiplied by a factor of 5.

## 3 COSEISMIC SLIP DISTRIBUTION

We jointly inverted the two types of available geodetic data described in the previous section to obtain the slip distribution of the Chi-Chi earthquake and we estimate the resolution of the inversion over the rupture surface.

### 3.1 Modelling approach and inversion method

The seismogenic zone is described by a surface of displacement discontinuities in isotropic homogeneous elastic half-space. Each dislocation is defined by the strike- and dip-slip components of slip and induces a surface displacement field estimated by the analytical solution of Okada (1985) for point sources. The final displacement field is obtained by summing the contributions of all elementary sources. Provided the fault geometry is fixed, all the geodetic data can be related to slip in each fault segment. The forward problem is thus linear and can be expressed in matrix form, given in Appendix A.

Previous studies (e.g. Ma *et al.* 2000; Chi *et al.* 2001; Ji *et al.* 2001; Johnson *et al.* 2001; Dominguez *et al.* 2003) modelled fault rupture with simplified geometry. In order to take into account a more realistic fault rupture, we imposed the complex geometry as described in Section 2.1 (Fig. 4). It is first based on the mapped rupture trace. At the extremity of the northern bend, the measured displacement of GPS site G098 (Fig. 5) indicates that it lies on the footwall of the fault rupture. We thus extended the east–west surface rupture to include this station within the footwall. Next, based on Suppe (1981, 1985, 1986), the central east–west cross-section of CTF fault rupture surface is described by a west-verging ramp connecting a 6 km deep flat to the surface. To the east, the fault dives again to 10 km depth. This ramp–flat–ramp structure was modelled by a polynomial curve, defined by the coordinates of its upper and its lower edges and the dip angles at its two extensions. We extrapolated this geometry laterally along the meridian portion of the fault. To the north, the fault rupture was described with similar curves connecting the northern bottom of the north–south fault portion to the northern surface bend with a steep southward dip-angle. In order to incorporate this description, we modified the analytical code improved by Flück *et al.* (1997). The set of the polynomial curves defines a grid of 23 100 triangular elements. We thus defined a fault surface, without any discontinuity or arbitrary segment, which takes into account the geological constraints. A dislocation is assigned to each triangle.

In order to limit the dimension of the models to the number of data, the triangular elements were arranged into 300 sets. Within each group, strike- and dip-slip components of the dislocations are equal. We performed the inversion using a weighted least squares method. Weighted misfits and the roughness of slip distribution were simultaneously minimized (Constable *et al.* 1987; Menke 1989). Smoothing was gradually strengthened until the predicted magnitude agrees with the seismological data. The method is presented in more detail in Appendix B.

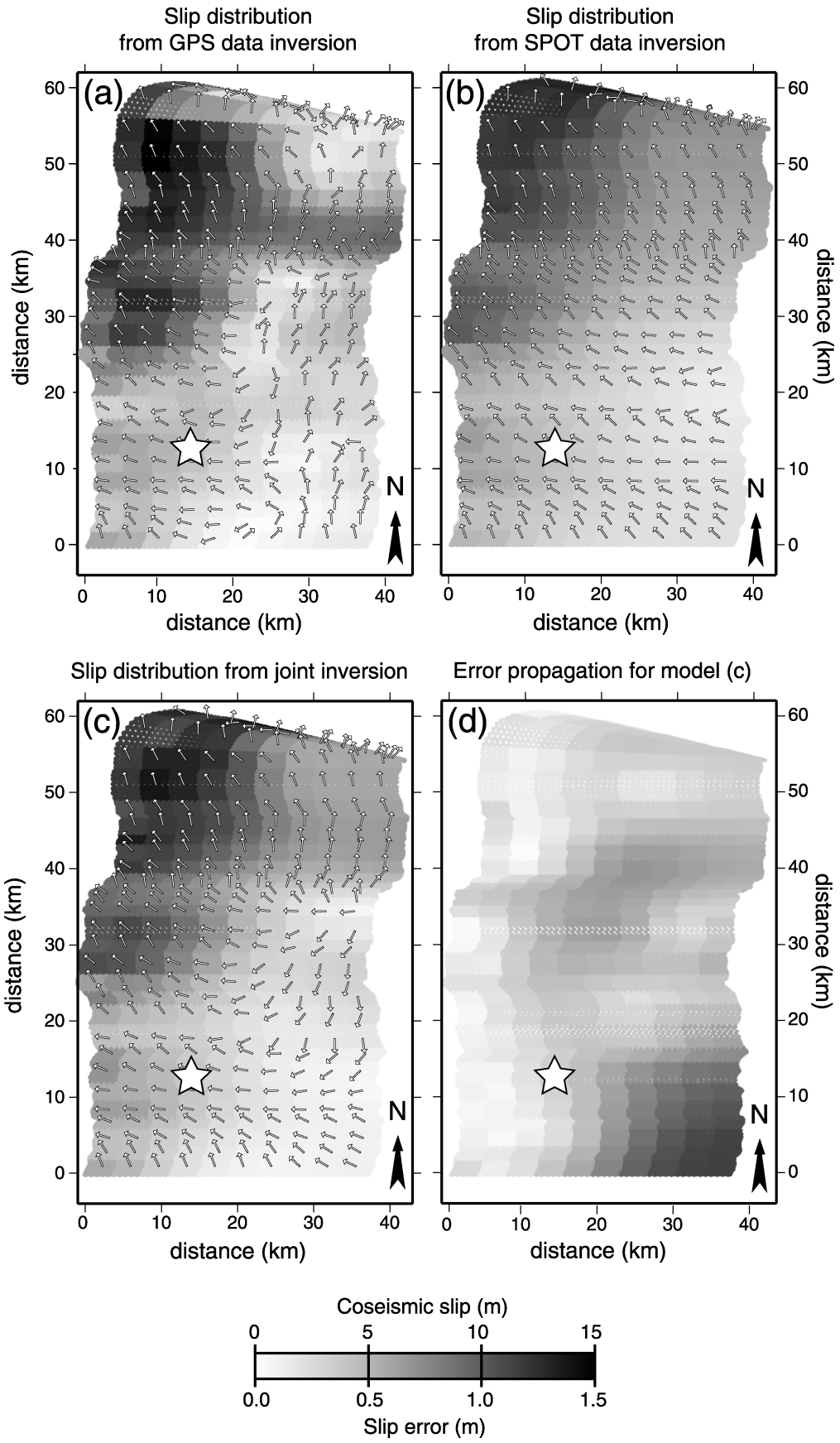


**Figure 6.** Modelled slip distribution, from inversion of (a) GPS data, (b) SPOT data and (c) from joint inversion. (d) Error propagation for the model c. White star represents the epicentre.

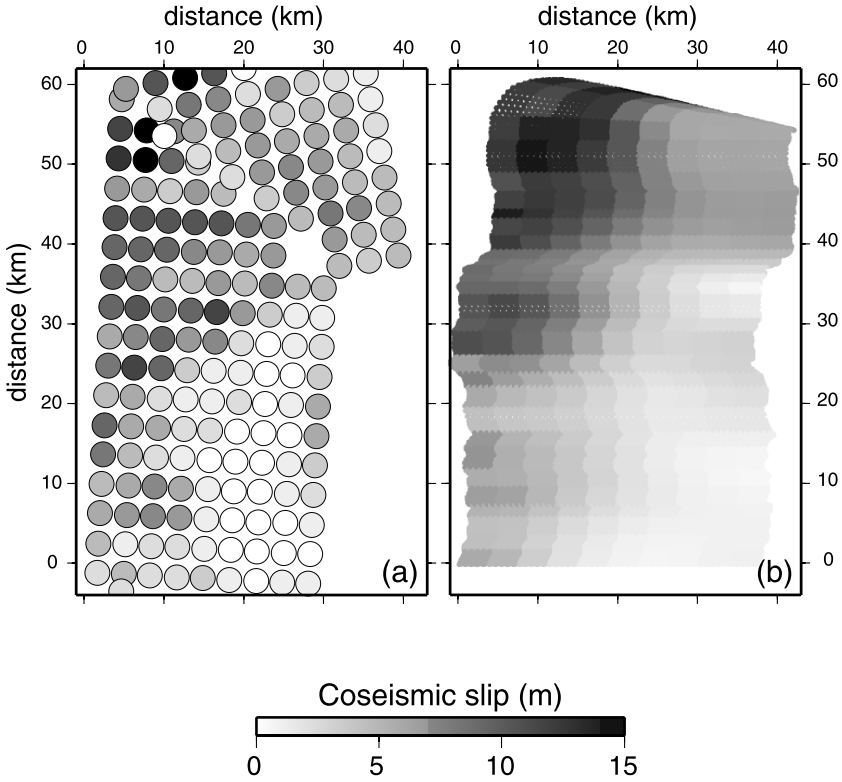


**Figure 7.** Comparison of (a) the model of coseismic slip distribution deduced from strong motion, teleseismic and GPS data by Ma *et al.* (2001) and (b) the model derived in this study. Note overlaps and holes in the modelled rupture plane of Ma *et al.* (2001).

### 3.2 Analysis of slip distribution and predicted surface displacements

#### *3.2.1 Distribution and resolution of coseismic slip*

The inversions of GPS measurements as well as SPOT data produced to the first order a slip amount that increases from the southern lower part of the fault to the northern upper edge with a maximum slip of approximately 15 m (Figs 6a, b and c). It occurs approximately along the China/Philippine convergence direction derived from interseismic GPS measurements (Yu *et al.* 1997). Whatever the data we inverted, most of the displacement is localized on the upper ramp and slip is clearly minor east of the hypocentre. In more detail, the slip distributions display two well-defined maxima to the north and one of little significance to the south. The GPS data inversion resulted in a very irregular slip distribution at depth, with abrupt azimuth changes (Fig. 6a), whereas the SPOT data inversion globally generated a smoother one (Fig. 6b). The combination of both data sets induced an intermediate slip distribution. The GPS measurements greatly influence the result of the combined inversion because, although they are much less numerous than the SPOT data, they are much more precise. The teleseismic data, alone or combined with strong motion, and GPS data led Ma *et al.* (2000) and Ma *et al.* (2001) to propose very similar models of coseismic slip distribution (Fig. 7). This coherence suggests the reliability of the results and enlightens the role of the geometry (the northern bend) taken into account in our modelling as well as in the study of Ma *et al.* (2000, 2001). The best-fitting double couple representation of the moment tensor obtained with the joint inversion of geodetic data is comparable to the Harvard solution (Fig. 8). However, it indicates a reverse fault plane more NE–SW, more steeply dipping to the SE, with a larger strike-slip component than the CMT. Our solution further illustrates the combination of slip along the north–south portion of the fault and its northern bend.

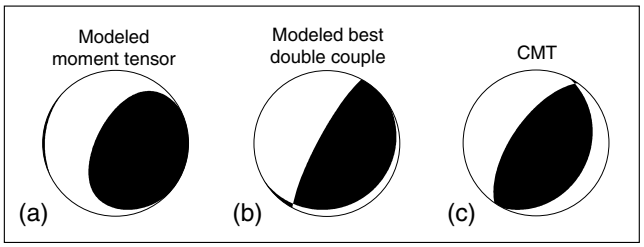


**Figure 8.** (a) Moment tensor and (b) best double couple inferred from our modelled seismogenic zone, and (b) CMT solution.

In contrast with the previous studies, we quantify the robustness of our model using the model resolution and the error propagation vector (Menke 1989). The model resolution determines how well the model parameters can be resolved. We defined this resolution for the joint inversion of GPS and SPOT data with the distributions of importance and 1-sharpness (Figs 9a and b), respectively the diagonal values and the number of elements significantly different from zero of the resolution matrix, as explained in Appendix D. The model parameters are more accurately resolved when these values, ranging from 0 to 1, both get close to 1. Model resolution sharply declines from west to east, i.e. with depth. As the surface displacements overlay the whole area above the seismogenic zone of the Chi-Chi earthquake, this decrease with depth expresses the increase of distance between measurements (confined at the surface of the Earth) and the deformation source, as previously noted by

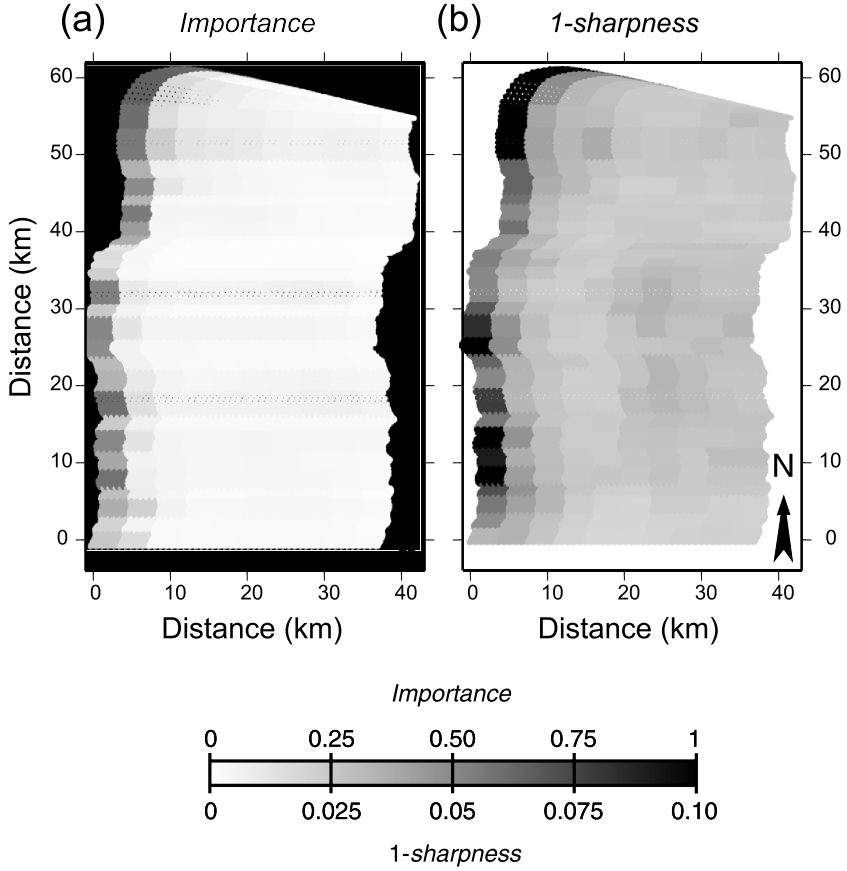


**Figure 9.** (a) Importance and (b) 1-sharpness of the resolution matrix for the combined inversion (see text and Appendix D for detailed definition). Model parameters are better resolved when both values get close to 1.

Árnadóttir & Segall (1994), Sagiya & Thatcher (1999) and Mazzotti *et al.* (2000). Such a decline with distance to the data positions is systematically expected for any slip modelling based on surface measurements and must be taken into account in the analysis of results. For the Chi-Chi earthquake we assumed that constraints are poor on the portion of the rupture below *ca* 7.5 km depth. Quantification of the model accuracy may also be inferred from the error propagation vector (Appendix C): propagation error illustrates again decreasing accuracy of the model with depth. Moreover, it indicates that the slip amount on the minimum displacement area to the southeast is the most imprecisely estimated, with a slip error greater than 1 m (Fig. 6d). In the next section, we will test the static stress triggering approach to compensate for this lesser reliability of our model at depth.

### *3.2.2 Predicted and residual surface displacements*

The histograms of the residuals (the differences between observed and predicted displacements; Figs 10a, b and c) demonstrate the fair agreement between observed and calculated displacements. This adjustment indicates that the ramp and flat geometry is in first order, consistent with the GPS and SPOT data. In the inversion based on GPS measurements only, most of the residuals are lower that 0.5 m, with at least 50 per cent of them below 0.1 m for both horizontal and vertical components (Fig. 10a). The mean values and the standard deviations of the residuals are respectively 0.23 and 0.48 for horizontal components and 0.22 and 0.42 for vertical ones. However, some of the data points are not explained with a better accuracy than 1 to 2.5 m. In the inversion of the SPOT data, the residual horizontal displacements are distributed in an asymmetric way with a mean value of 0.45 and $1\sigma = 0.45$, the largest values reaching 2 m (Fig. 10b). In the joint inversion, the distribution of the horizontal residuals is dominated by the adjustment to the much more numerous SPOT data (Fig. 10c) with a mean value of 0.52 and $1\sigma = 0.61$. The residuals of the vertical GPS displacements (mean value = 0.27 and $1\sigma = 0.53$) are weakly altered when SPOT measurements are included in the inversion.

We next examine the calculated and residual displacements induced by the combined inversion in the vicinity of the CTF (Figs 11 and 12). First both GPS and SPOT data are in first order, well adjusted. Next, GPS measurements are less precisely fitted along the fault trace on the hangingwall, vertical displacements are heterogeneously overestimated and only very few horizontal residuals are significant (Fig. 11). The vertical motion of the northern portion of the hangingwall is slightly underestimated. Our model properly accounts for the SPOT data (Fig. 12a). However, in more detail, it underestimates the northwestward displacements within a narrow band east of the fault trace and overestimates the northwestward motion of the northeast corner of the SPOT images.

One can expect that modifications at depth of our fault geometry, in particular to the northern and southern extremities where no geological constraints are available, could improve the adjustment to the data. However, the inversion for both slip distribution and fault geometry from surface displacements would require solving a nonlinear problem that is beyond the scope of this study. The analysis of

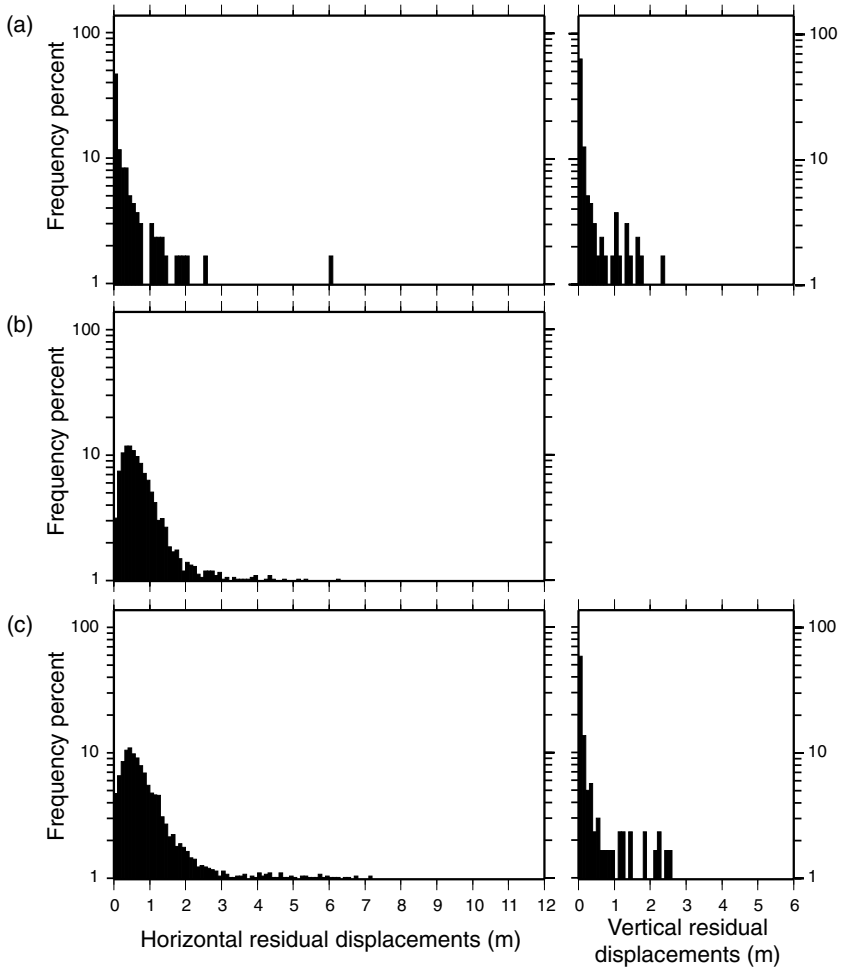


**Figure 10.** Histograms of the residual surface displacements, measured minus predicted displacements, for inversion of (a) GPS data, (b) SPOT data and (c) for joint inversion.

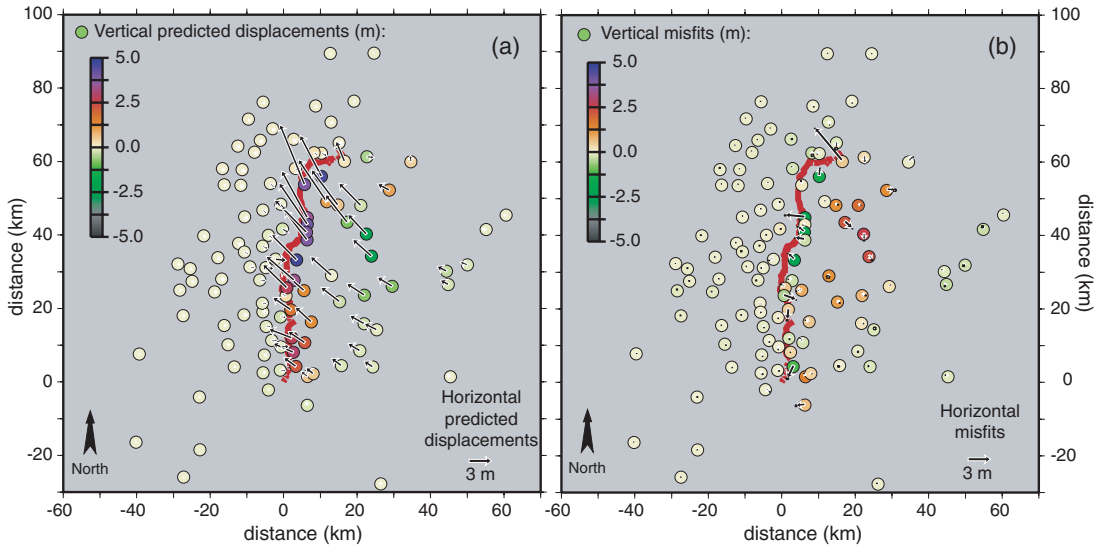


**Figure 11.** (a) Predicted and (b) residual GPS displacements for the joint inversion; black vectors for horizontal components and colored circles for vertical components.

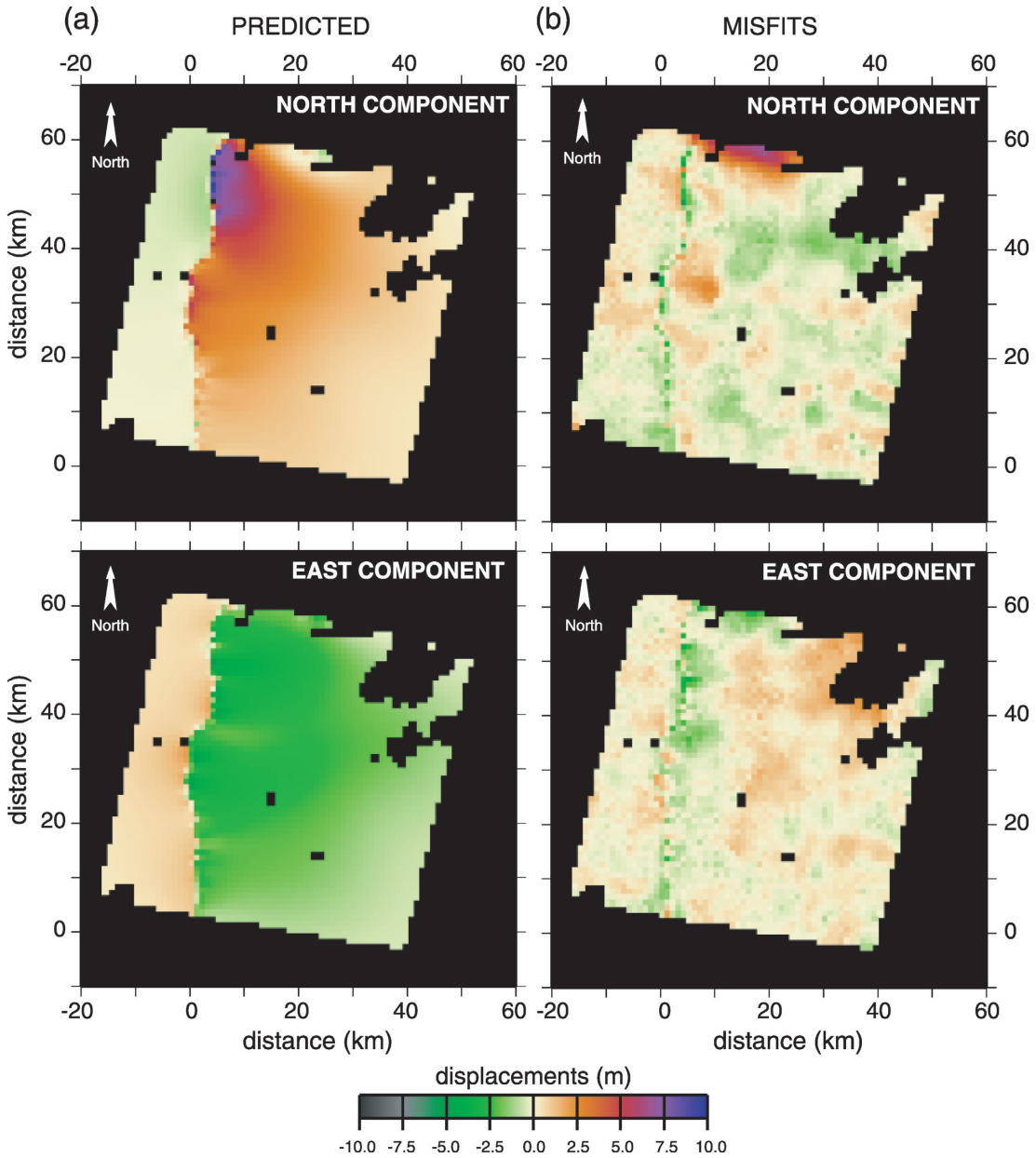


**Figure 12.** (a) Predicted and (b) residual SPOT displacements for the joint inversion.

the seismicity change in the next section aims to compensate for the decreasing resolution, but also to discuss the deep CTF geometry and thus to complement the inversion method.

## 4 STATIC STRESS TRIGGERING

In Section 3.2, we showed that the model resolution decreases with depth. We test our modelled seismogenic zone (slip distribution and geometry) using the seismicity change resulting from the Chi-Chi earthquake. It has been proposed that the distribution of Coulomb stress change can be used to predict the locations of triggered or reduced seismicity (Oppenheimer *et al.* 1988; King *et al.* 1994; Stein *et al.* 1994). In order to test our model with the seismicity change, we used this static stress triggering approach and thus compared the Coulomb stress change derived from our modelling with the variations of the earthquake distribution induced by the main shock.

### 4.1 Seismicity before and after the main shock

The Central Weather Bureau has recorded an important amount of seismological data over Taiwan with its dense network. A seismicity catalogue from 1991 to 2000, complete for magnitudes greater than $M_L = 2$, is available on the CD-ROM by Shin & Teng (2001). As a result of the variation of the seismic station network (number and sensitivity of the stations), a normalization of the earthquake production before and after the earthquake is required. We thus computed, rather than the seismicity rate, the earthquake density per volume unit, which is the number of earthquakes per volume unit normalized by the total number of earthquakes, along five east–west cross-sections (Fig. 13). The variations of earthquake density distributions before and after the Chi-Chi event indicate that the main shock considerably modified the spatial distribution of seismicity. Some pre-seismic patterns of

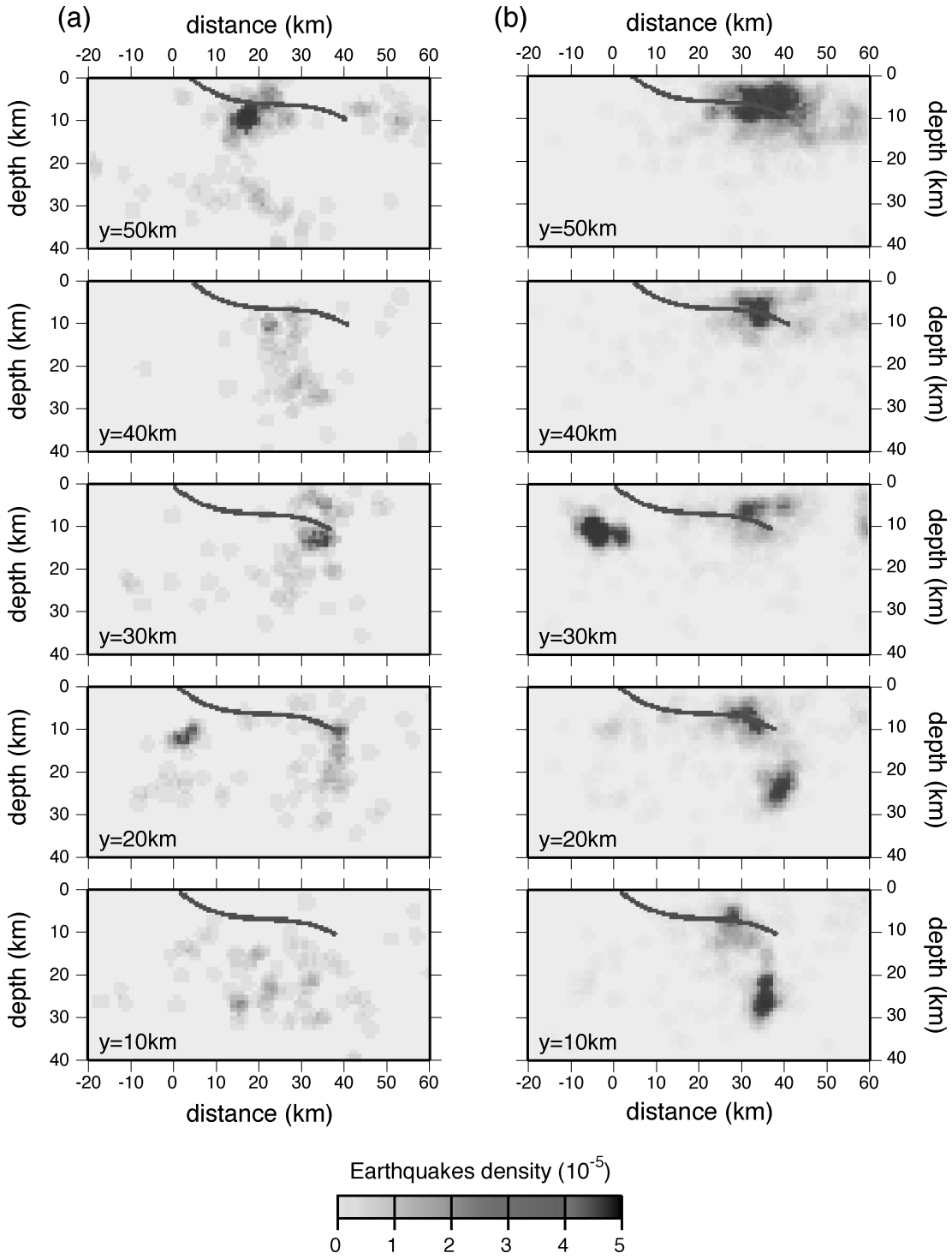


**Figure 13.** East–west earthquakes density cross-sections, (a) before and (b) after the Chi-Chi main shock: *y* values give the profiles position and black lines show the fault profiles.

seismicity disappeared after the main shock, whereas some new ones appeared.

### 4.2 Coulomb stress change estimation

We next calculated the Coulomb stress change resulting from the Chi-Chi earthquake to test whether it can predict the concentrations of aftershocks.

According to the Coulomb criterion, failure occurs on a plane when the Coulomb stress change on this plane, ΔCFF (Coulomb Failure Function), is positive

$$\Delta\mathrm{CFF} = \Delta\sigma_{\mathrm{S}} + \mu'\Delta\sigma_{\mathrm{N}}, \tag{1}$$

where $\Delta\sigma_{\mathrm{S}}$ and $\Delta\sigma_{\mathrm{N}}$ are respectively the shear and normal stress changes on the failure plane and $\mu'$ is the effective coefficient of friction, including the effects of pore-pressure changes.

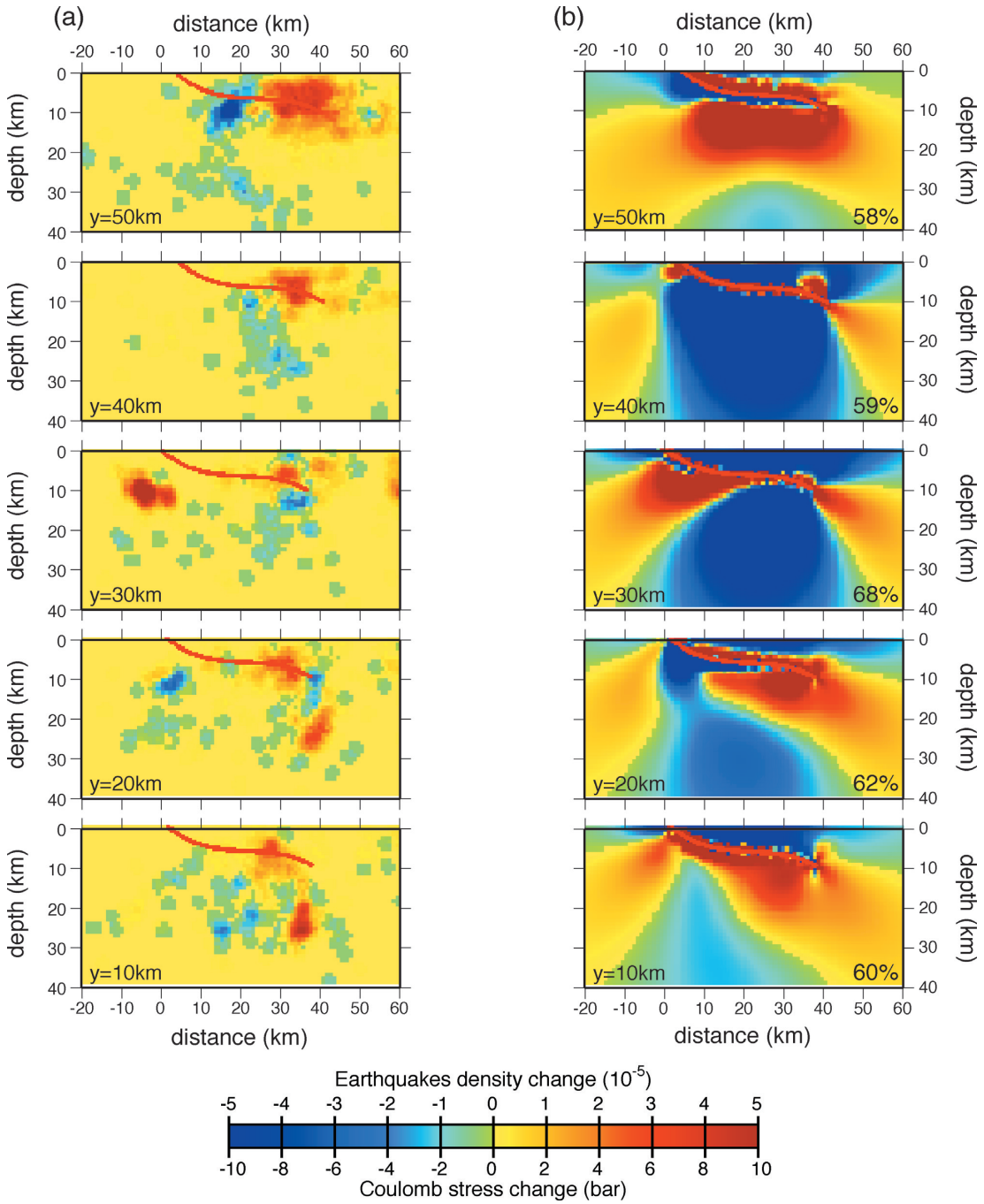


**Figure 14.** (a) Earthquakes density change and (b) Coulomb stress change induced by the main shock along east–west cross-sections: *y* values give the profiles position, percentages give the positive correlation amounts between (a) and (b) distributions, and red lines show the fault profiles.

The fault plane is optimally orientated (maximum Coulomb stress) when

$$\tan 2\beta = 1/\mu', \tag{2}$$

where $\beta$ is the angle of the plane with the greatest principal axis of the total stress tensor. King *et al.* (1994) presented in more detail the formulations used to calculate the optimally oriented planes and the Coulomb stress change.

Following this approach we compared the distribution of $\Delta$CFF, associated with our model, with the earthquake density changes, obtained from the difference between the density distributions after and before the main shock (Fig. 14a). The 3-D main shock induced stress tensors were derived from our coseismic slip model using the solution of Okada (1992). A 110°N compressive regional state of stress was introduced, as suggested by the interseismic GPS measurements (Yu *et al.* 1997). It was defined against the minimal vertical stress, taken to be lithostatic, by a uniform $10^8$ Pa deviatoric stress. The intermediate principal stress was chosen median. We tested whether introducing a deviator defined by Byerlee's law (Byerlee 1978) and taking the topographic effect into account lead to the same results. Static stress triggering applied to the Loma Prieta earthquake led Parsons *et al.* (1999) to conclude that the seismicity change is associated with shear stress change for major faults, while for minor faults, seismicity is concentrated where faults are

unclamped. Based on eq. (1), these results suggest a low $\mu'$ on major faults that develop a thick, impermeable gouge zone reducing sliding friction and a high $\mu'$ on minor faults. The high friction coefficient obtained by Seeber & Armbruster (2000) to better predict aftershocks of the Landers earthquake is consistent with the minor faults of the surrounding area. As we wished to describe the seismicity around the CTF, where faults most likely to slip are minor, we chose a high effective friction coefficient, $\mu' = 0.75$. However, we tested that a variation of $\mu'$ within the 0.4–0.75 range only slightly modifies the distribution pattern. The $\Delta$CFF was finally derived along five transects where the seismicity density change has been computed (Fig. 14b). A positive Coulomb stress change only indicates a tendency for slip on optimally oriented fractures in the same sense as the slip induced by the regional stress tensor. It does not take into account specific directions imposed by inherited structures such as the normal faults of the South China margin, pre-existing crustal fabric or faults parallel to the CTF. In spite of these limitations, the comparison of the $\Delta$CFF distribution with the earthquake density changes allowed us to test our model of the rupture zone.

### 4.3 Results

The distribution of Coulomb stress (Fig. 14b) change displays the commonly observed lobes at the fault extremities. However, the ramp and flat geometry and the sharp azimuth changes of our 3-D slip distribution complicates the pattern of the Coulomb stress change. Close to the fault rupture, the smoothed slip distribution still displays irregularities that cause peaks in stress. Coulomb stress change and seismicity display similar features. First, systematical positive $\Delta$CFF area is predicted in the western deep part, but the most important lobe precisely coincides with the swarm of earthquakes observed within the footwall on the central cross-section. Secondly, the area of positive stress change at the junction between the flat and the deeper ramp increases from centre to north in agreement with the seismicity. On the other hand, earthquake density diminution beneath the fault is globally predicted by static stress triggering.

In order to quantify how well our model respects the static stress triggering hypothesis, we calculated for each cross-section the amount of grid points where Coulomb stress and earthquake density change in the same sense. We only took into account the grid points for which earthquake densities before and after the main shock are significantly different. As a reference, the correlation for a random distribution is approximately 50 per cent and the best result previously obtained using a similar approach for different earthquakes is approximately 65 per cent of correlation, for example when applied to the 1994 Northridge earthquake (Stein 1999). For our model of the Chi-Chi earthquake, the correlation is significantly larger than random for the profile noted $y = 30$ km with 68 per cent and declines toward both extremities to 60 per cent (Fig. 14). The best result is thus obtained in the central part of the rupture where the ramp and flat structure was independently constrained and so indicates that our coseismic slip distribution is accurate even at depth in this area. Then, we investigated whether the correlation level could be used to constrain the fault geometry. We thus performed a similar calculation along the central profile ($y = 30$ km) with another geometry, characterized by a uniformly 15° dipping fault. The inferred Coulomb stress change (Fig. 15) is correlated to the earthquake density change at 64 per cent. Thus, the ramp and flat system provides an improvement of 4 per cent. However,

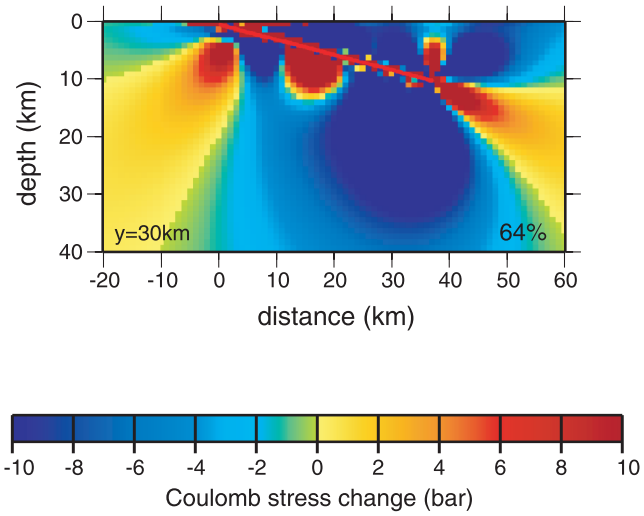


**Figure 15.** Coulomb stress change along the central east–west profile ($y = 30$ km) induced by the coseismic slip for a uniformly dipping fault.

this correlation variation is too low to extrapolate this result and to deduce that the decline towards the northern and southern extremities of the rupture is related to the less reliable fault geometry. Therefore, our seismogenic zone model is less appropriate in terms of static stress triggering to both extremities of the rupture, but we cannot determine whether the coseismic slip distribution at depth or the extrapolated ramp and flat system or both are less suitable. A systematic study of the various parameters or a non-linear inversion for the estimation of both slip distribution and geometry would be required: such a refined modelling is beyond the scope of this study and must be tested in a future paper.

## 5 RELAXATION TIME OF TRANSIENT POST-SEISMIC DEFORMATION INFERRED FROM SEISMICITY AND GPS OBSERVATIONS

As usually observed for large earthquakes, the evolution with time of the number and cumulative number of earthquakes displays a sudden increase triggered by the Chi-Chi event (Figs 16a and b): this aftershock sequence then decreased progressively. 260 days after the main shock, the largest aftershock ($M_L = 6.7$) induced a slight but clear signal. The slope of the cumulative earthquake variations, steeper at the end of the catalogue than during the pre-seismic period, reveals that the aftershock sequence was not yet over in 2000 December. We hereafter propose to examine this post-seismic decay of seismicity, compare this variation with the post-seismic GPS temporal series and deduce the implications for the post-seismic deformation processes.

### 5.1 Temporal seismicity variations

The empirical Omori law is often used to characterize the decay of aftershocks and is derived from his observations of aftershock of the 1891 Nobi earthquake. Dieterich (1994) formulated the readily observed influence of large earthquakes on temporal changes of seismicity rate, for both large and small earthquakes, as an effect of rate- and state-dependent friction. Seismicity is examined as a sequence of independent nucleation events. Transient changes, such as aftershocks, earthquake sequences or clustering, are interpreted

as a consequence of slip acceleration caused by stress perturbations. These modifications depend on slip and slip rate on the fault, and on time elapsed from the stress step (e.g. Toda *et al.* 1998; Stein 1999; Parsons 2002). In the absence of stress perturbation, the seismicity rate $r$ is supposed constant. After a sudden change induced by a stress step $\Delta\tau$, it recovers the steady state following a non-linear transient time dependence. Assuming a constant shear stress rate on the fault, the seismicity rate $R$ can be expressed as

$$R(t) = r/\{[\exp(-\Delta\tau/A\sigma) - 1]\exp(-t/t_a) + 1\}, \quad (3)$$

in which $A$ is a constitutive fault parameter, $\sigma$ is the total normal stress and $t_a$ is the characteristic relaxation time for the perturbation of earthquake rate. The maximum amplitude $R_0$ of this transient change is function of the stress step, eq. (3) can then be written as

$$R(t) = r/\{[(r - R_0)/R_0]\exp(-t/ta) + 1\}. \quad (4)$$

We first modelled the temporal seismicity change induced by the Chi-Chi main shock. We used the $M_L \geq 2.0$ earthquakes of the CWB catalogue within a 100 × 80 km area centred on the rupture plane. The background seismicity ($r = 0.7$ shocks/day) was inferred from the slope of the cumulative earthquakes number during the more than 8 yr recording period preceding the main shock (Fig. 16b). We then estimated the relaxation time of the transient effect together with its amplitude $R_0$ by fitting temporal variations of number and cumulative number of earthquakes with eq. (4). We found an 8–14 yr range (Figs 16a and b), consistent with the global study of Parsons (2002) for aftershocks of $M_S \geq 7.0$ earthquakes in larger scale areas. It is associated with an inversely correlated 350–800 shocks/day range. The best adjustment is for $t_a = 11$ yr associated with $R_0 = 500$ shocks/day (Fig. 17).

### 5.2 Post-seismic GPS measurements

Yu *et al.* (2001) have also used the Taiwan GPS network to recover the Chi-Chi post-seismic displacements field. The finite displacements of the first 3 months following the main shock are well fitted by after-slip that is mainly south and downdip of the coseismic slip (Bechor *et al.* 2001; Hsu *et al.* 2002). The model of Hsu *et al.* (2002) revealed significant slip on an 11–12 km deep decollement near the hypocentre of the main shock, but weak slip where large coseismic slip occurred.

The nearby continuous sites on the hangingwall display the transient displacement decrease during a 210 day long post-seismic period. Yu *et al.* (2001) adjusted these temporal variations with an exponential decay function with different amplitudes but one relaxation time of 86 ± 2 days between a site to the south of the hangingwall (I007, location in Fig. 5) and a site (S01R) in the Penghu archipelago, around 50 km west of Taiwan. However, Hsu *et al.* (2002) determined for the same baseline but for a longer period (approximately 450 days) a decay constant of 159 days. Moreover,

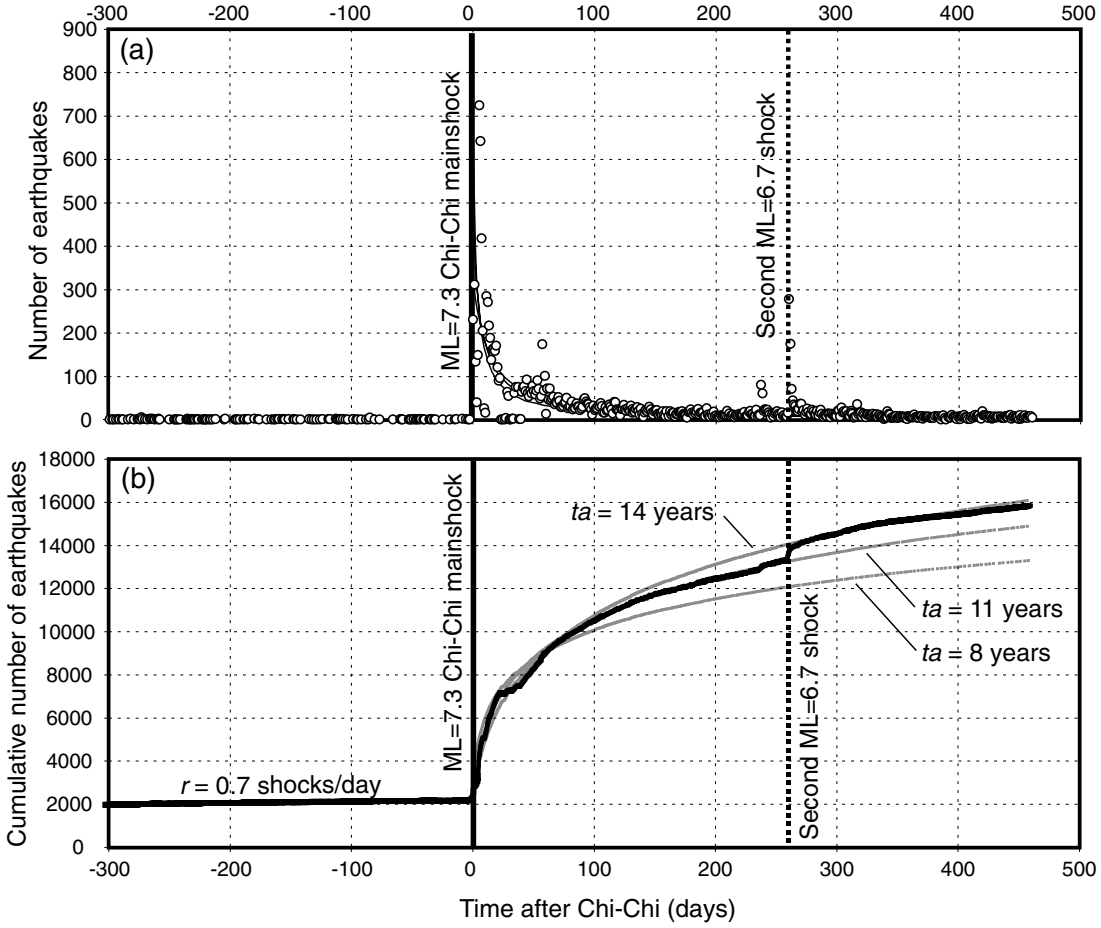


**Figure 16.** (a) Earthquake production (white circles) and (b) rate of earthquake production versus time (black line). These data are best fitted by the formulation of Dieterich (1994) (grey lines) for $t_a = 11$ yr and $R_0 = 500$ shocks/day. Chi-Chi main shock ($t = 0$) is highlighted with black lines, the largest aftershock, $M_L = 6.7$ ($t = 260$ days) with dotted lines.

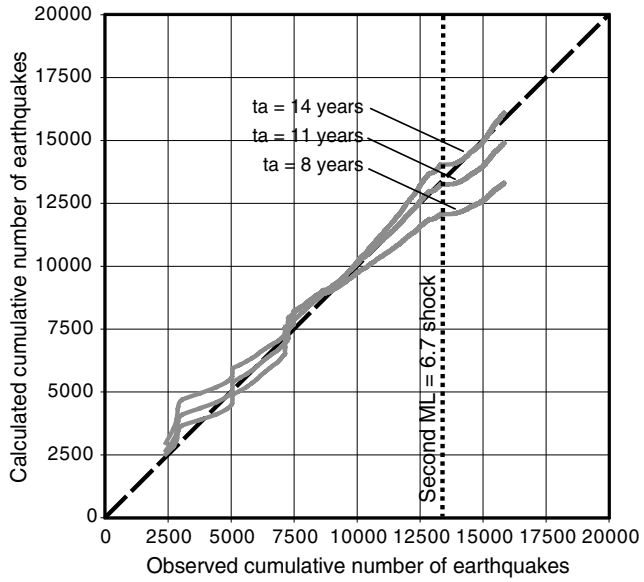


**Figure 17.** Correlation of calculated cumulative earthquake number with Dieterich's law with observed cumulative earthquake number (grey lines). The first bisector (dashed line) represents the perfect adjustment.

these authors estimated a relaxation time of 330 days north of the hangingwall and of 206 days over the footwall.

### 5.3 Implications for post-seismic relaxation time

The relaxation times of the aftershock sequence and post-seismic GPS displacements, respectively ranging from 8 to 14 yr and from $\frac{1}{4}$ to 1 yr, are significantly different. The 86 and 159 day values proposed by Yu *et al.* (2001) and Hsu *et al.* (2002) for the 210 and 450 day periods of GPS measurement respectively may indicate that the time window can have a large influence on the estimation of the relaxation time. Hsu *et al.* (2002) relied on a period as long as the available duration of seismicity, but GPS measurements, less sensitive, might require a longer recording.

The large discrepancy between the decays of earthquake rate and of post-seismic surface displacements, and the disagreement between the locations of aftershocks and the maximum after-slip (Hsu *et al.* 2002) imply that seismicity and surface deformation are driven by different physical processes.

## 6 DISCUSSION

GPS measurements, SPOT data, seismicity and geological observations were used to study both the coseismic slip distribution and the post-seismic relaxation of the Chi-Chi earthquake. Two aspects of the deformation related to this seismic event were developed. First, we modelled the coseismic slip distribution based on the geodetic surface displacements and attempted to test the model using the static stress triggering approach. Secondly, we examined the decay with time of the aftershock sequence triggered by the main shock in terms of relaxation time of post-seismic deformation.

As the Chi-Chi earthquake broke a subaerial structure and therefore is the most documented subduction earthquake, it offers the opportunity to derive an exceptionally well constrained model of the rupture and to better understand splay faults in such context. The high-quality data notably allowed to take into account the complex fault geometry inferred from geological studies and seismic profiles and to derive a model of slip distribution without any *a priori* information. For that, we developed, in contrast to previous studies, a new modelling of the seismogenic zone using the point source dislocation formulation (Okada 1985, 1992) that allows any fault geometry without discontinuity, nor artificial segment. By applying the weighted least-squares inversion method we estimated not only a model of slip distribution along the Chi-Chi surface rupture but also quantified its resolution.

Whereas subduction earthquakes more generally generate larger slip amount at depth than along the shallow portion of the seismogenic zone (e.g. Sagiya & Thatcher 1999; Salichon *et al.* 2003), the inversion of GPS and SPOT data, without any *a priori* information, resulted in an unusual distribution for the Chi-Chi event, with slip continuously increasing towards the northern upper corner of the fault. The large range of coseismic deformation measurements related to the Chi-Chi earthquake allowed various analysis of this event and so offered the opportunity to compare our results with other estimations of coseismic slip distribution. The fair agreement with previous models based on various data shows the reliability of this first-order description. Based on these results, we tested a synthetic model defined by a linearly increasing slip amount and a constant azimuth of slip vectors parallel to the plate convergence (305°N). We compared the surface displacements induced by this distribution with GPS and SPOT measurements. The histograms of residuals in Fig. 18 reveal a reasonable fit to the data. This simple model therefore represents a good approximation of the coseismic slip distribution for the Chi-Chi earthquake. Slip irregularities, for example the local maxima on the upper ramp, are necessary to fully

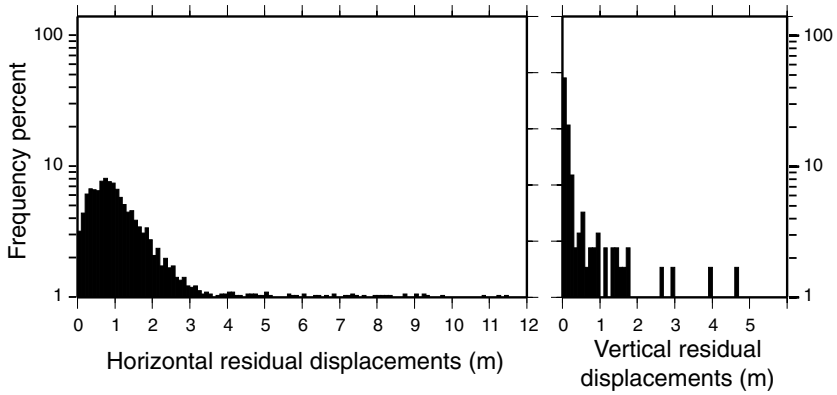


**Figure 18.** Histograms of the residual surface displacements, measured minus predicted displacements, for the synthetic coseismic slip distribution, linearly increasing towards the northern upper edge of the fault rupture and uniformly trending towards 305°N.

explain the surface displacements, but are of second order. One can wonder whether this simple pattern of coseismic slip distribution on the CTF is valid for splay faults over other subduction zones, but is not detected because of the lack of measurements above the upper portion of the seismogenic zone. Such feature would have important implications for estimating tsunami risk in subduction zones.

The resolution matrix led us to discuss in detail the reliability of our coseismic slip model. The resolution declines rapidly with depth because of increasing distance to the data points. As the inverted surface displacement field above the rupture plane of the Chi-Chi earthquake was exceptionally well documented, this quantification of the model resolution puts the emphasis on the limited reliability at depth of any slip estimation based on surface measurements only. This led us to examine seismicity as independent data to test our model following the static stress hypothesis. According to the correlation amount between Coulomb stress and seismicity changes, the seismogenic zone is accurately defined in the central part and gets less appropriate towards the southern and northern extremities. Bollinger et al. (submitted) showed for the Himalayan front that the topographic load is necessary to explain the seismicity using the static stress triggering approach. The large aftershock cluster along the front of the Central Range (Dominguez *et al.* 2003) suggests that including the topographic effects in the regional stress field might improve the correlation level.

The small variation of the correlation with the fault geometry suggests however that the static stress triggering approach is probably not precise enough to discuss in detail models of seismogenic zones and their geometry. A systematic analysis would be necessary to estimate precisely the sensitivity to fault parameters, for example based on the similar approach applied to an earthquake for which both coseismic slip and rupture geometry are well defined. Such a study is beyond the scope of this paper, but would allow to determine whether the seismicity is an appropriate data set to compensate for the poor resolution at depth of slip distribution models. If not, the static stress triggering approach might be only suitable to test the first-order characteristics of seismogenic zones or, as more commonly done, to explain the main features of the seismicity change as consequence of a slip distribution.

Finally, using Dieterich's law we estimated the relaxation time from aftershocks sequence. We found a relaxation time of 8–14 yr, significantly longer than those obtained from post-seismic GPS measurements. This discrepancy may be partly the result of the insufficiently long time windows used in GPS estimation, but mainly shows that the post-seismic deformation is driven by different processes, not all associated with aftershock production.

## ACKNOWLEDGMENTS

We are most grateful to Jean-Philippe Avouac for providing some guidance and numerous discussions during the course of this study. We thank John Suppe for enlightening us on the structure of the Chelungpu fault. We are also grateful to Kelin Wang for providing part of the computer routines used to model the coseismic displacements. We thank Ann-Sophie Provost for English improvement. We express our appreciation to the Editor Martyn Unsworth and two anonymous reviewers for their useful suggestions, comments and critical evaluation. Most figures were generated using the GMT software (Wessel & Smith 1995). This research was supported by Collège de France and CNRS UMR 8538 (France).

## REFERENCES

Árnadóttir, T. & Segall, P., 1994. The 1989 Loma Pieta earthquake imaged from inversion of geodetic data, *J. geophys. Res.,* **99**, 21 835–21 855.

Bechor, N., Segall, P., Hsu, Y. J. & Yu, S.B., 2001. Time-depended inversion for post-seismic slip following the 1999 Chi-Chi Taiwan earthquake using GPS observations, *EOS, Trans. Am. geophys. Un.,* **82**, 47.

Bollinger, L., Avouac, J.P., Cattin, R. & Pandey, M.R., 2004. Stress build up along the Himalayan Megathrust, *J. geophys. Res.,* submitted.

Byerlee, J.D., 1978. Friction of rock, *Pure appl. Geophys.,* **116**, 615–626.

Chen, Y.-G., Chen, W.-S., Lee, J.-C., Lee, Y.-H., Lee, C.-T., Chang, H.-C. & Lo, C.-H., 2001. Surface rupture of the 1999 Chi-Chi earthquake yields insights on active tectonics of Central Taiwan, *Bull. seism. Soc. Am.,* **91**(5), 977–985.

Chi, W.-C, Dreger, D. & Kaverina, A., 2001. Finite-Source Modeling of the 1999 Taiwan (Chi-Chi) Earthquake derived from a Dense Strong Motion Network, *Bull. seism. Soc. Am.,* **91**(5), 1144–1157.

Constable, S.C., Parker, R.L. & Constable, C.G., 1987. Occam's inversion: a practical algorithm for generating smooth models from electromagnetic sounding data, *Geophysics,* **52**(3), 289–300.

Dieterich, J.A., 1994. Constitutive law for rate of earthquake production and its application to earthquake clustering, *J. geophys. Res.,* **99**(2), 2601–2618.

Dominguez, S., Avouac, J.-P. & Michel, R., 2003. Horizontal coseismic deformation of the 1999 Chi-Chi earthquake measured from SPOT satellite images: implications for the seismic cycle along the western foothills of Central Taiwan, *J. geophys. Res.,* **108**(2), 2083, doi: 10.1029/2001JB000951.

Flück, P., Hyndman, R.D. & Wang, K., 1997. Three-dimensional model for great earthquakes of the Cascadia subduction zone, *J. geophys. Res.,* **102**, 20 539–20 550.

Hsu, Y.-J., Bechor, N., Segall, P., Yu, S.-B., Kuo, L.-C. & Ma, K.-F., 2002. Rapid afterslip following the 1999 Chi-Chi, Taiwan, earthquake, *Geophys. Res. Lett.,* **29**(16), 1754, doi: 10.1029/2002GL014967.

Ji, C., Helmberger, D.V, Song, T.-R., Ma, K.-F. & Wald, D.J, 2001. Slip distribution and tectonic implication of the 1999 Chi-Chi, Taiwan, earthquake, *Geophys. Res. Lett.,* **28**(23), 4379–4382.

Johnson, K.M, Hsu, Y.-J., Segall, P. & Yu, S.-B., 2001. Fault geometry and slip distribution of the 1999 Chi-Chi, Taiwan earthquake imaged from inversion of GPS data, *Geophys. Res. Lett.,* **28**, 2285–2288.

Kelson, K.I., Kang, K.-H, Page, W.D., Lee, C.-T. & Cluff, L.S., 2001. Representative Styles of Deformation along the Chelungpu Fault from the 1999 Chi-Chi (Taiwan) Earthquake: Geomorphic Characteristics and Responses of Man-Made Structures, *Bull. seism. Soc. Am.,* **91**(5), 930–952.

King, G.C P., Stein, R.S & Lin, J., 1994. Static stress changes and the triggering of earthquakes, *Bull. seism. Soc. Am.,* **84**(3), 935–953.

Lee, J.-C., Chu, H.-T., Angelier, J., Chan, Y.-C., Hu, J.-C., Lu, C.-L. & Rau, R.-J., 2002. Geometry and structure of northern surface ruptures of the 1999 Mw = 7.6 Chi-Chi Taiwan earthquake; influence from inherited fold belt structures, *J. Struct. Geol.,* **24**(1), 173–192.

Lin, A., Ouchi, T., Chen, A. & Maruyama, T., 2001. Nature of the fault jog inferred from a deformed well in the northern Chelungpu Surface rupture zone, related to the 1999 Chi-Chi, Taiwan, ML 7.3 earthquake, *Bull. seism. Soc. Am.,* **91**(5), 959–965.

Loevenbruck, A., Cattin, R. Le Pichon, X., Courty, M.-L. & Yu, S.-B., 2001. Seismic cycle in Taiwan derived from GPS measurements, *Comptes Rendus Acad. Sci.,* **333**, 57–64.

Ma, K.-F., Lee, C.-T., Tsai, Y.-B., Shin, T.-C. & Mori, J., 1999. The Chi-Chi, Taiwan earthquake; large surface displacements on an inland thrust fault, *EOS, Trans. Am. geophys. Un.,* **80**(50), 605–611.

Ma, K.-F., Song, T.-R.A, Lee, S.-J. & Wu, H.-I., 2000. Spatial slip distribution of the September 20, 1999, Chi-Chi, Taiwan, earthquake (Mw = 7.6); inverted from teleseismic data, *Geophys. Res. Lett.,* **27**(20), 3417–3420.

Ma, K.-F., Mori, J., Lee, S.-J. & Yu, S.-B., 2001. Spatial and temporal distribution of slip for the 1999 Chi-Chi, Taiwan, earthquake, *Bull. seism. Soc. Am.,* **91**(5), 1069–1087.

Mazzotti, S., Le Pichon, X., Henry, P. & Miyazaki, S.-I., 2000. Full interseismic locking of the Nankai and Japan-west Kurile subduction zones: An analysis of uniform elastic strain accumulation in Japan constrained by permanent GPS, *J. geophys. Res.,* **105**, 13 159–13 177.

Menke, W., 1989. *Geophysical data analysis: discrete inverse theory,* Academic Press, San Diego, California.

Okada, Y., 1985. Surface deformation due to shear and tensile faults in a half-space, *Bull. seism. Soc. Am.,* **75**, 1135–1154.

Okada, Y., 1992. Internal deformation due to shear and tensile faults in a half-space, *Bull. seism. Soc. Am.,* **82**, 1018–1040.

Oppenheimer, D.H, Reasenberg, P.A. & Simpson, R.W., 1988. Fault plane solutions for the 1984 Morgan Hill, California, earthquake sequence: Evidence for the state of stress on the Calaveras fault, *J. geophys. Res.,* **93**, 9007–9026.

Ouchi, T., Lin, A., Chen, A. & Maruyama, T., 2001. The 1999 Chi-Chi (Taiwan) earthquake: earthquake fault and strong motions, *Bull. seism. Soc. Am.,* **91**(5), 966–976.

Parsons, T., 2002. Global Omori-law decay of triggered earthquakes: large aftershocks outside the classical aftershock zone, *J. geophys. Res.,* **107**(9), 2199, doi: 10.1029/2001JB000646.

Parsons, T., Stein, R.S, Simpson, R.W. & Reasenberg, P.A., 1999. Stress sensitivity of fault seismicity; a comparison between limited-offset oblique and major strike-slip faults, *J. geophys. Res.,* **104**(9), 20 183–20 202.

Pathier, E., Fruneau, B., Deffontaines, B., Angelier, J., Chang, C.-P., Yu, S.-B. & Lee, C.-T., 2003. Coseismic displacements of the footwall of the Chelungpu fault caused by the 1999, Taiwan, Chi-Chi earthquake from InSAR and GPS data, *Earth planet. Sci. Lett.,* **212**, 73–88.

Rubin, C.M., Sieh, K., Chen Y.-G, Lee J.-C, Chu, H.-T, Yeats, R., Mueller, K. & Chan, Y.-C., 2001. Surface Rupture and Behavior of Thrust Fault Probed in Taiwan, *EOS, Trans. Am. geophys. Un.,* **82**(47), 565–569.

Sagiya, T. & Thatcher, W., 1999. Coseismic slip resolution along a plate boundary megathrust: The Nakai Trough, souwest Japan, *J. geophys. Res.,* **104**, 1111–1129.

Salichon, J., Delouis, B., Lundgren, P., Giardini, D., Costantini, M. & Rosen, P., 2003. Joint inversion of broadband teleseismic and interferometrix syntherix aperture radar (InSAR) data for the slip history of the Mw = 7.7, Nazca ridge (Peru) earthquake of 12 November 1996, *J. geophys. Res.,* **108**, 2085, 10.1029/2001JB000913.

Seeber, L. & Armbruster, J.G., 2000. Earthquakes as beacons of stress change, *Nature,* **407**(6800), 69–72.

Shin, T.-C. & Teng, T.-L., 2001. An overview of the 1999 Chi-Chi, Taiwan earthquake, *Bull. seism. Soc. Am.,* **91**(5), 895–913.

Stein, R.S., 1999. The role of stress transfer in earthquake occurrence, *Nature,* **402**(6762), 605–609.

Stein, R.S., King, G.C.P. & Lin, J., 1994. Stress triggering of the 1994 M = 6.7 Northridge, California, earthquake by its predecessors, *Science,* **265**, 1432–1435.

Suppe, J., 1981. Mechanics of mountain building and metamorphism in Taiwan, *Geol. Soc. China Mem.,* **4**, 67–89.

Suppe, J., 1985. *Principles of structural geology,* Prentice-Hall, Inc., Englewood Cliffs, NJ.

Suppe, J., 1986. Reactivated normal faults in the western Taiwan fold-thrust belt, *Geol. Soc. China Mem.,* **7**, 187–200.

Toda, S., Stein, R.S, Reasenberg, P.A, Dieterich, J.H. & Yoshida, A., 1998. Stress transferred by the 1995 Mw = 6.9 Kobe, Japan, shock; effect on aftershocks and future earthquake probabilities, *J. geophys. Res.,* **103**(10), 24 543–24 565.

Van Puymbroeck, N., Michel, R., Binet, R., Avouac, J.-P. & Taboury, J., 2000. Measuring earthquakes from satellite images, *Appl. Optics.,* **39**(20), 3486–3494.

Wessel, P. & Smith, W.H.F., 1995. New version of the Generic Mapping Tools released, *EOS Trans. AGU,* **76**, 329.

Yu, S.-B., Chen, H.-Y. & Kuo, L.-C., 1997. Velocity field of GPS stations in the Taiwan Area, *Tectonophysics,* **274**, 41–59.

Yu, S.-B., Kuo L.-S., Hsu Y.-J., Su, H.-H., Liu, C.-C., & Hou C.-S., 2001. Preseismic deformation and coseismic displacements associated with the 1999 Chi-Chi, Taiwan, earthquake, *Bull. seism. Soc. Am.,* **91**(5), 995–1012.

## APPENDIX A: FORWARD MODELLING

We assumed that the seismogenic zone may be described by a surface of displacement discontinuities in an isotropic homogeneous elastic half-space. The strike- and dip-slip components of the sources can be written as the $M$ parameters of the model vector $\mathbf{m}$. Similarly, the components of surface displacements were denoted by $\mathbf{d}$, a vector of $N$ data. As long as the fault geometry is fixed, all the geodetic data can be related to slip in each fault segment. The forward problem is thus linear and can be expressed in the matrix form

$$\mathbf{d} = \mathbf{Gm}, \tag{A1}$$

where $\mathbf{G}$ is the matrix of Green functions for each fault segment calculated from the solution of Okada (1985) for an elementary point source.

## APPENDIX B: INVERSION METHOD

In order to limit the dimension of the models to the number of data, the triangular elements were arranged into 300 sets. Within each group, strike- and dip-slip components of the dislocations are equal. We performed the inversion with a least-squares method minimizing the functional $F$, simultaneously taking into account the weighted misfits and the roughness of the slip distribution (Constable *et al.* 1987; Menke 1989):

$$F(\mathbf{m}) = \lambda||\mathbf{W}(\mathbf{Gm} - \mathbf{d})||^2 + ||\boldsymbol{\partial}_1\mathbf{m}||^2 + ||\boldsymbol{\partial}_2\mathbf{m}||^2. \tag{B1}$$

$\mathbf{W}$ is the $N \times N$ diagonal weighting matrix composed by the inverse of the uncertainties. $\boldsymbol{\partial}_1$ and $\boldsymbol{\partial}_2$ are the $M \times M$ operators for the smoothing, quantified by the difference between slip components of two adjacent point sources along the strike and dip of the fault surface. The Lagrange multiplier $\lambda$ controls the relative emphasis assigned to this smoothing. $\lambda$ is obtained by gradually reducing the model roughness versus data misfit until the predicted magnitude agrees with the seismological data. This regularization procedure leads to a larger misfit, but prevents unreasonable distribution of slip vectors striking in all directions with huge norms. The minimum of $F$ is obtained for

$$\mathbf{m} = \mathbf{G}^{-\mathbf{g}}\mathbf{d}, \tag{B2}$$

where $\mathbf{G}^{-\mathbf{g}}$ is the $M \times N$ matrix such as

$$\mathbf{G}^{-\mathbf{g}} = \left\{\lambda^{-1}\left(\boldsymbol{\partial}_1^{\mathrm{T}}\boldsymbol{\partial}_1 + \boldsymbol{\partial}_2^{\mathrm{T}}\boldsymbol{\partial}\right) + (\mathbf{WG})^{\mathbf{T}}\mathbf{WG}\right\}^{-1}(\mathbf{WG})^{\mathbf{T}}\mathbf{W}. \tag{B3}$$

## APPENDIX C: ERROR PROPAGATION

The error propagation vector $\mathbf{P}$ provides an estimation of the errors on the $M$ model parameters

$$\mathbf{P} = \mathbf{G}^{-\mathbf{g}}\mathbf{E}, \tag{C1}$$

where $\mathbf{E}$ is the vector of the $N$ data uncertainties.

## APPENDIX D: RESOLUTION MATRIX

To estimate how well the model parameters can be resolved, we derived the $M \times M$ resolution matrix $\mathbf{R}$ (Menke 1989)

$$\mathbf{R} = \mathbf{G}^{-\mathbf{g}}\mathbf{G}. \tag{D1}$$

If **R** is the identity matrix, the model is perfectly determined. Otherwise, the computed model parameters are weighted averages of the true parameters. The graphs of the row elements against column indices thus describe the resolutions of each parameter. Sharp peaks with maximum values centred about the main diagonal, **R** close to the identity matrix, indicate a reasonably resolved model. The model resolution is thus useful in determining what significance can be assigned to the results. We computed for each raw of **R**, that is for each model parameter, the diagonal values and the number of elements significantly different from zero normalized to the matrix size, respectively called the importance and the sharpness. Importance and 1-sharpness are both ranging between 0 and 1 and tend to 1 when the model parameter tends to get completely resolved.